

Journal of Biomedical Optics

SPIEDigitalLibrary.org/jbo

Vessel orientation-dependent sensitivity of optoacoustic imaging using a linear array transducer

Stefan Preisser
Nigel L. Bush
Andreas G. Gertsch-Grover
Sara Peeters
Arthur E. Bailey
Jeffrey C. Bamber
Martin Frenz
Michael Jaeger

Vessel orientation-dependent sensitivity of optoacoustic imaging using a linear array transducer

Stefan Preisser,^a Nigel L. Bush,^{b,c} Andreas G. Gertsch-Grover,^b Sara Peeters,^a Arthur E. Bailey,^d Jeffrey C. Bamber,^{b,c} Martin Frenz,^a and Michael Jaeger^a

^aUniversity of Bern, Institute of Applied Physics, Sidlerstrasse 5, 3012 Bern, Switzerland

^bInstitute of Cancer Research and Royal Marsden NHS Foundation Trust, Joint Department of Physics, Downs Road, Sutton, Surrey, SM2 5PT, United Kingdom

^cInstitute of Cancer Research and Royal Marsden NHS Foundation Trust, CRUK-EPSC Cancer Imaging Centre, Downs Road, Sutton, Surrey, SM2 5PT, United Kingdom

^dScitech Instruments Inc., 2826 Crestlynn Pl., North Vancouver, BC, V7J 2S5, Canada

Abstract. For clinical optoacoustic imaging, linear probes are preferably used because they allow versatile imaging of the human body with real-time display and free-hand probe guidance. The two-dimensional (2-D) optoacoustic image obtained with this type of probe is generally interpreted as a 2-D cross-section of the tissue just as is common in echo ultrasound. We demonstrate in three-dimensional simulations, phantom experiments, and *in vivo* mouse experiments that for vascular imaging this interpretation is often inaccurate. The cylindrical blood vessels emit anisotropic acoustic transients, which can be sensitively detected only if the direction of acoustic radiation coincides with the probe aperture. Our results reveal for this reason that the signal amplitude of different blood vessels may differ even if the vessels have the same diameter and initial pressure distribution but different orientation relative to the imaging plane. This has important implications for the image interpretation, for the probe guidance technique, and especially in cases when a quantitative reconstruction of the optical tissue properties is required.

© 2013 Society of Photo-Optical Instrumentation Engineers (SPIE) [DOI: [10.1117/1.JBO.18.2.026011](https://doi.org/10.1117/1.JBO.18.2.026011)]

Keywords: photoacoustic imaging; ultrasound imaging; linear array; free hand; real time; imaging plane; *in vivo*; vascular imaging; limited view.

Paper 12624R received Sep. 20, 2012; revised manuscript received Jan. 3, 2013; accepted for publication Jan. 14, 2013; published online Feb. 6, 2013.

1 Introduction

Imaging plays a key role in medical diagnosis of vasculature disease. A widely used imaging modality is echo ultrasound (US) that displays grayscale (B-mode) images of anatomical detail based on the different US backscattering coefficients of various tissue types, allowing, for example, the evaluation of cardiovascular disease risks.¹ In addition to that Doppler and power Doppler sonography provide functional information of blood flow, which is important, for example, in liver diagnosis or in echocardiography.²⁻⁶ In comparison to computed tomography or magnetic resonance imaging, echo US has the advantage of being real-time, portable, and relatively inexpensive. In spite of these advantages echo US has often limited use due to difficulties in differential diagnosis: the B-mode image may fail to accurately identify diseased tissue or disease margins,⁷⁻⁹ and Doppler sonography is highly susceptible to motion artifacts and fails in detecting small blood vessels with slow blood flow.^{10,11} Therefore, it is widely recognized that echo US would strongly benefit if combined with further supplementary contrast modalities for a multimodal, and thus more accurate, diagnosis.

An ideal candidate that can complement vascular US imaging with additional functional information is optoacoustic imaging (OAI) that shows optical absorption based on the detection of US that is thermo elastically generated when irradiating the tissue with pulsed laser light.^{12,13}

One of the main tissue chromophore in the near infrared window used for deep imaging is hemoglobin.^{14,15} OAI, therefore, has the potential for high-contrast imaging of vascular and microvascular systems,¹⁶ and it has already shown promise for the detection of small tumors or diagnoses of vascular diseases.¹⁷⁻²³ In addition, functional imaging of varying blood oxygenation levels using a multispectral approach is feasible due to the pronounced differences in the absorption spectra of oxyhemoglobin and deoxyhemoglobin,^{24,25} which opens a wide clinical application field because blood oxygenation level and vessel growth are important indicators for tissue repair and tumor diagnoses.²⁶⁻³² Since OAI entails US detection, it can share the same acoustic probe with echo US and can readily be implemented in a combined system.²¹

Much of the benefits and flexibility of conventional US rely on its real-time display while free-hand scanning using hand-held probes. Consequently, real-time OAI is required for optimum diagnostic value in a combined system. This enables the display of the optically absorbing structures within the anatomical context shown in B-mode echo US, e.g., by overlaying of the two modalities in a manner similar to the display of color Doppler US.^{33,34} High signal-to-noise ratio and clinically useful deep imaging in OAI are only achieved with high laser pulse energy limiting the pulse rate to typically 10 Hz due to laser safety regulations. For real-time imaging, a combined system must therefore be capable of parallel receiving on all elements of an US array probe to display a complete image after every

Address all correspondence to: Martin Frenz, University of Bern, Institute of Applied Physics, Sidlerstrasse 5, 3012 Bern, Switzerland. Tel: +41 31 631 8943; Fax: +41 31 631 3765; E-mail: frenz@iap.unibe.ch

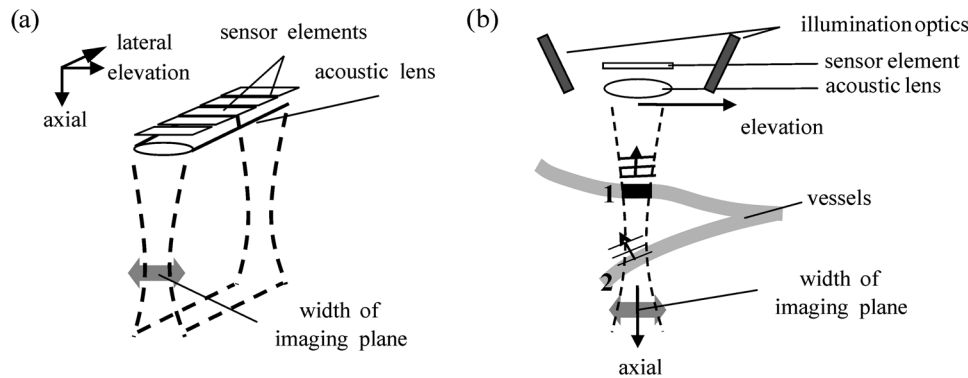


Fig. 1 (a) Sketch of a linear array probe, consisting of an array of acoustic sensors. A cylindrical acoustic lens in front of the array provides a narrow angular sensitivity profile in the elevation direction, thus predominantly a thin tissue slice is imaged, defined by the array axis in lateral direction and by the axial direction (axis of maximum sensitivity). (b) Blood vessels emit anisotropic cylindrical US transients. If the portion of the vessel that is located in the imaging plane is oriented in a way such that it radiates toward the array aperture (marked with 2), it is detected less sensitively or not at all depending on the angular sensitivity of the transducer. A change of the probe inclination such that the vessel is perpendicular to the axial direction of the transducer can make 2 visible.

single laser pulse. Due to technical limitations, this can currently only be achieved with one-dimensional (e.g., linear) probes because of the high element count of two-dimensional (2-D) arrays.^{35,36} A linear array (LA) probe contains a line of US sensors [Fig. 1(a)], which is highly directional in elevation y perpendicular to the array line x . Therefore, mainly acoustic sources located in a thin tissue slice, the imaging plane, are detected and show up on the resulting 2-D image.

The use of an LA probe has important implications on what information can be contained in the resulting optoacoustic image. For quantitative functional imaging, it is important that the pixel gray level can be related to the local density of absorbed laser energy in the imaging plane.^{37–39} It has been shown that an accurate reconstruction of the absorbed energy density is possible if signals are detected two-dimensionally resolved on a surface that encompasses the tissue sample (sphere, cylinder).^{40–42} When measurements are only available on a line, an accurate reconstruction is only possible when two conditions are fulfilled: first, the scan line has to encompass the sample and second, the laser light has to be confined to a plane parallel to this line (light sheet illumination). This is done in optoacoustic sectional imaging of weakly scattering targets, such as the zebra fish, drosophila pupa, or earthworm.^{43,44}

However, in clinical combined OAI with US, these requirements are not fulfilled. The limited aperture of a linear array probe on one side of the tissue leads to limited view artifacts, such as the appearance of a blood vessel as two arcs that delineate the upper and lower vessel boundary whereas the lateral boundary is missing.^{45,46} Such artifacts that distort the shape of an object may be acceptable for functional imaging as long as the signal amplitude quantitatively represents the amount of energy absorbed by the object.

Much more influential is that the irradiating light cannot be focused into a plane. Strong optical scattering leads to wide illumination of an extended volume of the tissue sample and thus a three-dimensional (3-D) distribution of the absorbed energy.¹³ It is sometimes implicitly assumed that with a narrow detectivity of the probe in a plane, an accurate reconstruction (apart from limited view artifacts) of the optical absorbers in this plane is still possible.^{47,48} This would then allow a quantitative reconstruction of parameters that are reflected in the absolute

amplitude, such as total hemoglobin concentration or the concentration of a contrast agent.

However, we demonstrate in this paper that this assumption is not valid in vascular OAI using an LA probe with plane detectivity. The reason for this is that the signal amplitude of a blood vessel is determined not only by the optical absorption, but equally important by the spatial orientation of the vessel relative to the imaging plane. Optical absorption in the cylindrically shaped blood vessel causes the coherent emission of a well-defined cylindrical transient that propagates mainly perpendicular to the blood vessel orientation.⁴⁹ This anisotropic acoustic radiation affects the detectability of the vasculature when an LA probe is used for OAI as shown in Fig. 1(b). Blood vessels are most sensitively detected when they are oriented such that the cylindrical transient propagates parallel to the imaging plane (marked with 1). When blood vessels are oriented with an angle relative to the axial direction of the imaging plane (marked with 2) this may lead to the propagation of the acoustic transients out of the imaging plane such that the vessels cannot be detected. Therefore the optoacoustic signal amplitude of blood vessels measured with a linear transducer array is not only determined by the local fluence rate and absorption coefficient but also by the inclination angle of the LA probe relative to the blood vessels' direction.

To investigate this angle dependence experimentally we scanned a blood vessel phantom under different probe inclination angles and compared the results to realistic simulations. In addition, *in vivo* mouse experiments were performed to evaluate the influence of the probe inclination on the imaging outcome in real tissue.

2 Materials and Methods

2.1 System Description

Phantom measurements were performed using a combined optoacoustic and echo US laboratory system based on an IMAGIC Sigma 5000 medical US scanner (Fukuda Denshi Switzerland AG, Basel). A linear probe (5-12LA, Fukuda Denshi) was used, containing 128 elements with an element pitch of 0.3 mm, having a central frequency of 7.5 MHz and a 7 MHz bandwidth (–3 dB). The system acquires signal data from 64 elements in

parallel during a 10 μs interval after each single laser pulse, resulting in an optoacoustic data frame corresponding to a field of view of 19.2 mm width and 15 mm depth range. A Q-switched Nd:YAG laser (VersaPulse, Coherent, USA) with a wavelength of 1064 nm, a repetition rate of 10 Hz, a pulse duration of 15 ns, and a pulse energy of 60 mJ was used for optoacoustic US generation.

For the *in vivo* mouse experiments we used a z.one™ (Zonare Medical Systems Inc., USA) US scanner, operated in a dedicated research mode, and a L10-5 linear array transducer (Zonare) with 128 elements on a 0.3 mm pitch, a central frequency of 7.5 MHz, and 5 MHz (−3 dB) bandwidth. Like with the Fukuda Denshi system, signal data from 64 elements could be digitized simultaneously after each single laser pulse, covering an aperture of 19.2 mm. However, a larger depth range of several centimeters could be obtained, which was only limited by US and optical attenuation. For optoacoustic generation, we used a custom-built Q-switched Nd:YAG laser (ELEN, Italy) at 1064 nm wavelength, with 30 mJ pulse energy and a pulse length of about 7 ns.

2.2 Scanning Procedure

The elongated shape of the individual sensors in the elevation direction, in combination with a cylindrical acoustic lens in front of the linear transducer, creates a narrow sensitivity profile in the elevation direction. The imaging plane is defined by the line of transducer elements in lateral direction and the axial direction of maximum sensitivity [Fig. 1(a)].

The spatial orientation of the linear probe determines the position and orientation of the imaging plane inside the tissue. The position and orientation can be varied either by shifting the probe on the skin surface, rotating it about the axial direction, or by rotating the probe about the array axis. The last does not change the position of the probe on the tissue surface but the angle between the tissue surface and the axial direction of the imaging plane. This is henceforth referred to as an inclination change.

The influence of the blood vessel orientation on the relative signal amplitude can best be perceived when scanning the vessel structure in a 3-D way and under various different probe inclinations (Fig. 2). For this purpose, the linear array transducer was mounted on a probe holder, which allowed a manual adjustment of the inclination angle by rotation about the array axis. The probe holder was mounted on a motorized linear stage (T-series, Zaber, Canada) for scanning perpendicular to the array axis. The

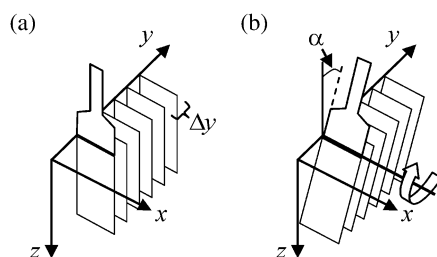


Fig. 2 (a) Sketch of the scan procedure at an inclination angle α of 0 deg to acquire a 3-D volume of the scan object. The Cartesian lab coordinates are shown, as well as the rectangular image planes for each scan position and the scan step size Δy . (b) Sketch of the scan procedure for an inclination angle α different from 0 deg. The Cartesian lab coordinates are independent from the inclination angle. To allow a match between the different inclination angles, the 3-D image stack from each angle was scan-converted to the Cartesian lab coordinates.

probe was placed on the phantom or mouse with the array axis parallel to the transversal plane ($x - y$) of the scan object. Then the sample was mechanically linear scanned parallel to the sagittal plane ($y - z$) in steps Δy of 0.25 mm over a range y of 65 mm for the phantom scan respectively 60 mm for the mouse. At each position, an optoacoustic image of the scan object was acquired with a single-laser pulse. This was done for various inclination angles α . For each inclination angle α , the successive 2-D images of a scan were then stacked to form a 3-D volume. We performed scans using inclination angles ranging from -30 deg to $+30$ deg in 10 deg steps to obtain seven 3-D volumes. Loss of acoustic contact between the Mylar foil and the probe in the phantom experiment and mechanical constraints in the mouse experiment prevented scanning at larger angles. To allow a match between the different inclination angles, the 3-D image stack from each angle was scan-converted to the Cartesian lab coordinates: x : dimension parallel to array axis, y : scan direction, z : depth perpendicular to x and y .

2.3 Phantom Experiments

The phantom consisted of an entangled polyurethane tubing structure (internal diameter 0.3 mm) wrapped in a supporting structure made of cardboard [Fig. 3(a)]. To model optical absorption inside blood vessels, the tubing could be filled with an aqueous solution of India ink (Lefranc & Bourgeois, France). An absorption coefficient of 6 cm^{-1} (measured with transmission photometry) at the illumination wavelength of 1064 nm was chosen. Whereas the illumination wavelength was dictated by the available laser equipment, the absorption coefficient was deliberately chosen so as to realistically mimic venous blood in the whole wavelength range between 650 and 900 nm, which is preferably used for deep OAI. To mimic the surrounding tissue, the tubing was embedded in a 16% gelatin solution containing 1 g/l TiO_2 for optical scattering, resulting in a reduced scattering coefficient of 2.6 cm^{-1} .^{50,51} To complete the phantom, a latex skin was added to prevent desiccation and to provide mechanical stability [Fig. 3(b)]. The optical absorption coefficient of water at 1064 nm is 0.18 cm^{-1} ; the effective attenuation coefficient of the gelatin medium was therefore 1.2 cm^{-1} , which is in the range of breast tissue.

The phantom was placed upright in a water tank (14 cm height, 18 cm width, 3.5 cm thickness) constructed from Perspex, with two large optical and acoustic windows, one at the front and one at the rear side of the tank, made of Mylar foil (thickness $3 \mu\text{m}$) [Fig. 3(c)]. For irradiation, the laser beam was coupled into an 8 mm diameter optical fiber bundle (Volpi AG, Switzerland) and guided to one of the two windows to illuminate the sample. The linear array probe was acoustically coupled to the opposite Mylar window using US gel. Transmission mode was chosen for two reasons: first, the probe and the illuminating fiber bundle could be moved independently using two remote-controlled motorized linear stages (T-series, Zaber, Canada) for optimum illumination of the imaging plane, and second, the transmission mode operation avoided optoacoustic clutter that is generally associated with reflection mode operation.³³

2.4 Simulation of the Phantom Experiment

Prior to embedding the artificial vessel structure, a sequence of photographs was taken while rotating the structure about its

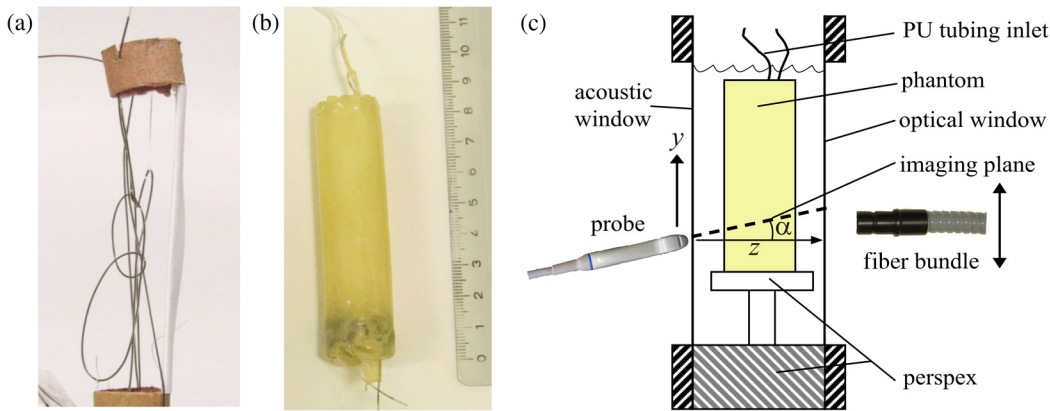


Fig. 3 (a) Polyurethane tubing structure, filled with India ink solution. (b) The completed gelatin phantom, covered with a latex skin. (c) Sketch of the phantom experiment setup.

longitudinal axis. Figure 3(a) shows one picture out of that sequence. The three-dimensional arrangement of the vessels was determined based on this image sequence. The optoacoustic signal was then simulated using a custom-built time-domain simulation code. This code calculated the optoacoustic signal under 3-D wave propagation using well-known analytic expressions.^{49,52} To realistically simulate the receive properties of an element out of an array probe, the element was divided up into a grid of point sensors that were spaced closely enough as to adequately sample the signal that could be detected under the transducers' frequency response. The signal of a single element was then calculated as the integral over all point sensors making up that element, and the signal detected by the linear probe was calculated in the same way for each element. In that way, elevation and lateral receive characteristics of the probe could be accounted for. The signals from all elements were then finally convolved with the element's impulse response. A linear array probe containing 64 elements was simulated in that way with specifications identical to the experimental system. To analyze effects of vessel orientation independent from a varying fluence distribution, the latter was assumed to be constant over the entire depth of the phantom resulting in a constant initial pressure generated all over the vessel structure.

We simulated optoacoustic images for the different transducer positions along the scan (y) direction for the inclination angles corresponding to the experiment. The same scan-conversion as used in the experiment was used to calculate the 3-D maps.

2.5 In Vivo Mouse Experiments

The nude mouse (CD1 nude female) experiments were conducted at the Institute of Cancer Research in London (ICR), United Kingdom, and all procedures for this study were approved by the ICR's local ethical board. The *in vivo* setup, shown in Fig. 4, entailed placing the mouse on a heating pad (Vevo Imaging Station, VisualSonics, Canada). The mouse was anesthetized with 2% isoflurane, added to one l/min 99.5% medical oxygen using an anesthesia system (matrix VIP 3000). The heart rate was monitored throughout the procedure. For acoustic coupling to the imaging system, an open water bag made of cling film suspended by a plastic ring was placed on the mouse after covering the skin with a thin layer of US gel for acoustic coupling. Care was taken not to entrap any air bubbles between the foil and the skin surface. The mouse

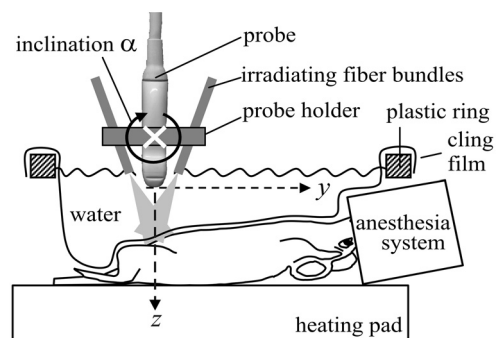


Fig. 4 Sketch of the experimental setup for *in vivo* nude mouse measurements. The mouse was anaesthetized and placed on the heating pad for temperature control. A temperature-controlled water bag was placed on top of the mouse and acoustically coupled to it with a thin layer of US gel. The linear transducer was submerged in the water, mounted on a rotatable probe holder, which also included the fiber optic bundles.

body temperature was monitored by a rectal thermometer and stabilized at 39°C by controlling the temperature of the heating pad and of the water bath.

Since the heating pad prevented access to the backside of the mouse, the *in-vivo* experiment had to be performed in reflection mode, with both irradiation and detection from the top. For this purpose a custom-made, bifurcated fiber optic bundle with line profile converters at the distal ends (Fiberoptic, Switzerland) was used for irradiation. The profile converters were mounted on either side of the probe, parallel to the linear probe axis, and uniformly irradiated an area of 20 by 5 mm on the skin surface, resulting in a radiant exposure of 30 mJ/cm² which was well below the ANSI safety limit.⁵³ More detailed information on the probe holder can be found elsewhere.⁵⁴ During the scan, the combined probe was submerged in the water bag.

3 Results

Sagittal projections of the 3-D maps ($y-z$ plane) illustrate that the optoacoustic amplitude from the gelatin phantom depends on the probe inclination angle in both the experimental and the simulation results (Fig. 5). The general behavior was identical: the individual images reveal that predominantly vessels orientated perpendicular to the probe's axial direction (indicated with dashed lines) were detected. This led to the visibility of

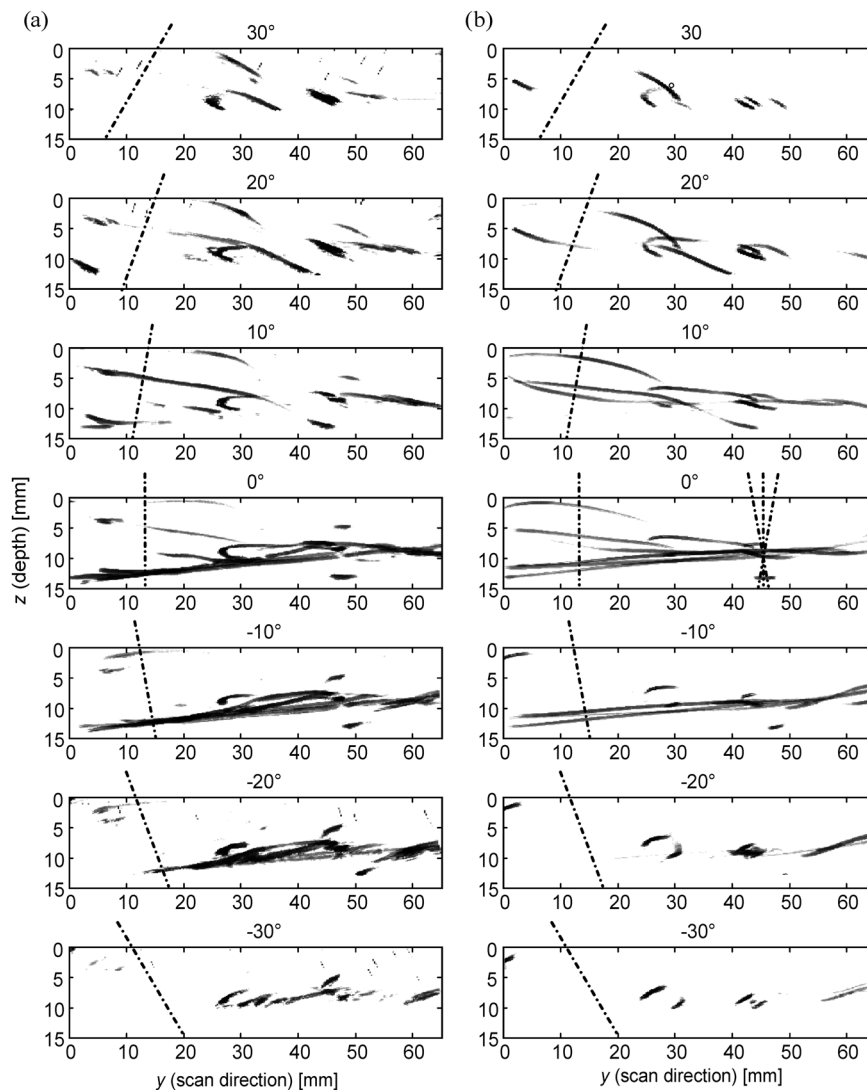


Fig. 5 Sagittal projections of the 3-D maps of the reconstructed OA signal for the various probe inclination angles. Left column: Phantom experiment. Right column: Phantom simulation. Dashed lines indicate the orientation of the imaging plane. Mainly vessels perpendicular to the orientation of the imaging plane are detected. Additional dashed lines in the 0 deg angle figure to the right indicate the location and orientation of the imaging plane for the OA B-mode results shown in Fig. 6.

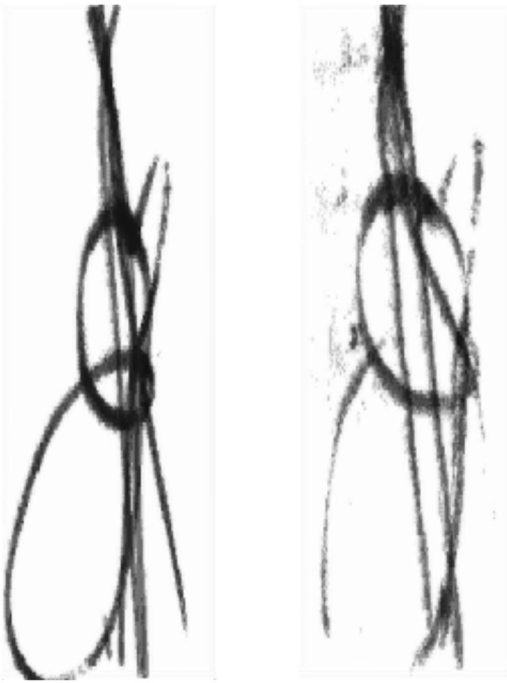
different segments of the vessel structure depending on the inclination angle.

In the simulation the diameter of the 0.3 mm inner diameter tubes was broadened to ~ 0.5 mm. This can be explained by the effect of the OA image point spread function, which had a full width half maximum of 0.3 mm in lateral direction (determined by the element pitch) as well as in axial direction (determined by the impulse response, 1.5 cycles at 7.5 MHz center frequency). In the experimental images the diameter was even broader, ~ 0.7 mm. This additional broadening will be addressed in the discussion section. In addition we would like to draw attention to the fact that the vessel structure must have been slightly twisted about the longitudinal phantom axis during the embedding process, something that can be observed when comparing the vessel geometry between experiment and simulation.

Because different segments of the vessel structure are visible when imaged at different inclination angles, a combination of the different results allows a more complete display of the vessel structure (Video 1). This combined display of all inclination angles shows a more complete picture and also reveals even

more clearly the twisting of the structure that occurred during the embedding process.

Clearly, a superposition of multiple inclination angle scans can provide a more complete 3-D image of the vessel structure but involves complex motion control and image registration. More importantly, it is not real-time and is susceptible to motion artifacts. Real-time and free-hand clinical OAI is best performed in a B-mode imaging mode, where a single 2-D B-mode image is displayed at a time. Figure 6 therefore shows simulated OA B-mode images that illustrate how the image changes when the same vessels are detected at a constant position but under different inclination angles. The location of the imaging plane for the three different inclination angles is indicated in the sagittal projection for angle 0 deg in Fig. 5. The intersection line of the three imaging planes was chosen at 9.5 mm image depth where the vessels marked with 1 to 4 in Fig. 6(b) (angle 0 deg) were located. Vessels 1 to 4 were oriented nearly perpendicular to the imaging plane, and consequently, the image shows the narrow intersection region with each vessel. The vessel marked with 5 is perpendicular to the axial direction of the transducer



Video 1 Superposition of the 3-D maps obtained with different probe inclinations yields a more complete view of the vessel structure. This is illustrated in this display of the 3-D volume (MPEG video, 0.2 MB) [URL: <http://dx.doi.org/10.1117/1.JBO.18.2.026011.1>] of the phantom simulation (left) and of the phantom experiment (right).

but intersects the imaging plane obliquely, so that the intersection region appears elongated. Vessels 1 to 4 in Fig. 6(b) appear as double dots in the 2-D optoacoustic images. This appearance is a combined effect of the limited bandwidth of the transducer and of the limited aperture of the linear array. The limited bandwidth acts as a spatial band-pass filter such that only the vessel surface can be seen. Was it not for the limited view of the linear array aperture, this would result in vessels 1 to 4 showing up as full circles. However, only the solid angle of the cylindrical transient detected by the limited aperture of the linear probe contributes to the reconstructed image. Therefore, only the front and back boundary of the cylindrical structures can be seen.

Much more importantly and independent from the limited view artifacts, the results in Fig. 6 illustrate the consequences of the inclination angle dependence of the signal amplitude by comparing the three inclination angle images. A change of the inclination angle altered the amplitudes of the different vessels

individually, determined by the orientation of the vessels relative to the imaging plane. By changing the inclination from 0 deg to +10 deg the vessels marked with 2 and 4 vanished while the relative weight of 1 and 3 was maintained [Fig. 6(a)], whereas at the -10 deg angle mainly 2 and 4 could be seen [Fig. 6(c)]. The strongest signal from each vessel was detected when oriented perpendicular to the imaging plane. Consequently, blood vessels that intersect the imaging plane at a different angle are not reconstructed with the same signal amplitude although they have the same initial pressure amplitude in the simulation [Fig. 6(b)]. By changing the inclination angle from 0 deg to 10 deg the vessels marked with 2, 4, and 5 do not appear in the reconstruction any more. In the image at the -10 deg angle, however, the vessels marked with 2 and 4 have higher signal amplitude compared with the 0 deg angle image.

In comparison to the phantom results where we obtained a clear image of the vessel structure, the results from the *in vivo* experiments were less well resolved. A coronal view, as opposed to the sagittal projections, was used for the display of these *in vivo* results to improve visibility of connected vessel structures. Coronal sections obtained at two different imaging depths are shown in red in Figs. 7 and 8. To provide anatomical context, the OA data are underlain with corresponding US coronal sections. On the right of each of these figures, the three different inclination angles are shown on a sketch of the mouse, along with the depth of the coronal plane and the scan direction. Note that the US coronal sections in Figs. 7 and 8 are displayed for the full probe aperture of 38.4 mm, whereas the limited receive aperture for OA imaging covered only 19.2 mm. Therefore, in Figs. 7 and 8, OA data are only available for the middle 19.2 mm of the x -axis. Also, OA contrast is only observed between 0 and 40 mm of the y -axis (scan direction) in Fig. 8. The missing data above 40 mm may be explained by the strong acoustic attenuation inside the lungs.

Different parts of the vascular structures are accentuated at different angles as illustrated in Fig. 7 when changing the inclination angle from +20 deg to -20 deg. In Fig. 7, the vessels near the surface of the thorax are distinctly imaged. These superficial vessels run nearly parallel to the skin surface and, thus, at roughly a constant angle to the probe. For this reason, the vessels are best imaged at the 20 deg and 0 deg inclination angles because the mouse lay at approximately a 10 deg angle oblique to the scan direction. At -20 deg inclination, the angle between the wave propagation direction and the imaging plane was too large for these vessels to be detected. Some residual dot-like features are seen, potentially where the cylindrical symmetry

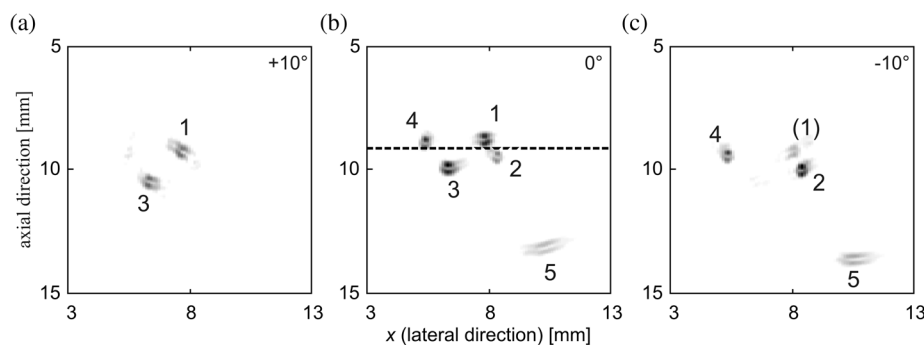


Fig. 6 Magnified view of OA B-mode images of the simulated vessel phantom at three different inclination angles. The orientation and location of the imaging planes was indicated in Fig. 5. The intersection line of the three image planes was chosen at roughly 9.5 mm depth (indicated with a dashed horizontal line in the 0 deg angle picture). The inclination angle was (a) +10 deg, (b) 0 deg, and (c) -10 deg.

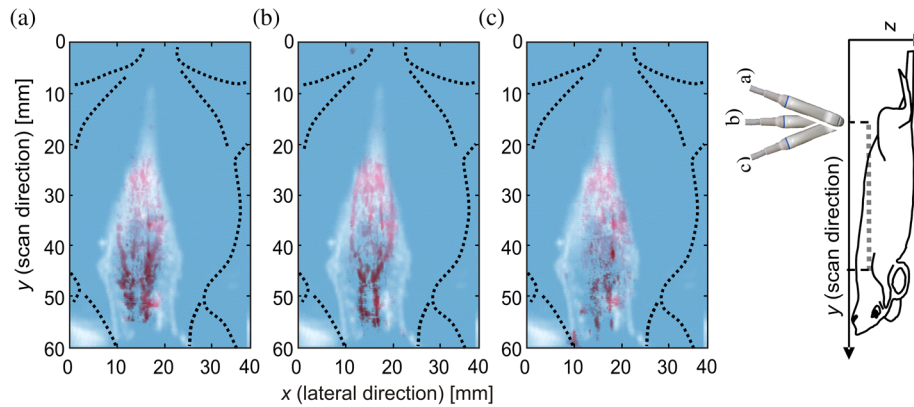


Fig. 7 Coronal section (depth 6.1 mm) of the thresholded OA data (red color in the online version, dark gray in the printed version) overlain with corresponding section of the US data (blue color scale in the online version, bright grayscale in the printed version) for different inclination angles, (a) +20 deg, (b) 0 deg, and (c) -20 deg. The sketch on the right side shows the depth of the coronal plane (gray dotted line), the scan direction, and the three different inclination angles.

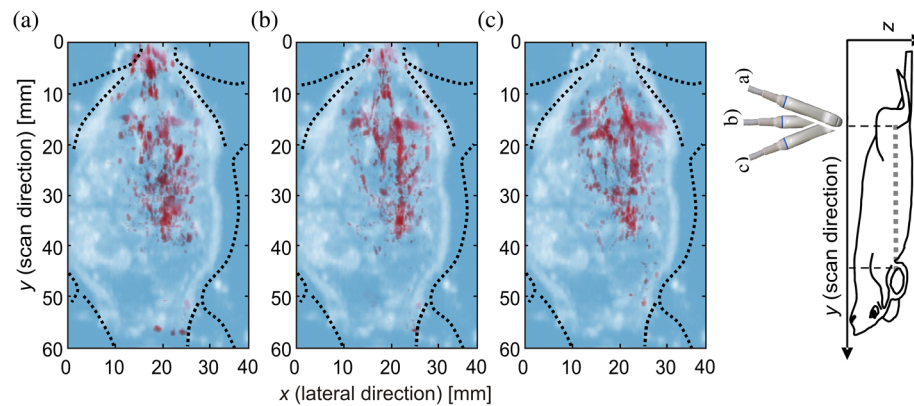


Fig. 8 Coronal section (depth 11.3 mm) of the thresholded OA data (red color in the online version, dark gray in the printed version) overlain with corresponding section of the US data (blue color scale in the online version, bright grayscale in the printed version) for different inclination angles, (a) +20 deg, (b) 0 deg, and (c) -20 deg. The sketch on the right side shows the depth of the coronal plane (gray dotted line), the scan direction, and the three different inclination angles. Note that OA data are only available from 10 to 20 mm in the lateral dimension (x) owing to the limited receive aperture. The absence of OA data between 40 and 60 mm in scan direction (y) may be explained with the strong acoustic attenuation inside the lungs which were located here.

of the wave front was broken due to an irregularity in the vessel shape. The same behavior is also observed in Fig. 8; however, it is more difficult to identify connected vessels at this greater depth, and the influence of the inclination angle is perceived primarily as a gross change of the detected structures.

4 Discussion

In all three cases, the simulation, the phantom experiment, and the *in vivo* experiment, we successfully demonstrated that vascular optoacoustic imaging using linear probes depends significantly on the inclination angle at which the vessel structure is scanned. The vessels must be approximately perpendicular to the transducer's direction of reception to be sensitively detected (Figs. 5 and 7). Especially the good agreements between experimental and simulated images of the vessel tree phantom in Fig. 5 demonstrates that the anisotropic US emission of the vessels together with the receive properties of the linear array transducer fully explain the extent of the angular dependence of the optoacoustic signal. The *in vivo* experiment confirms the influence of the inclination angle as well, but the interpretation of the

results is somewhat more challenging. A distinct influence of the angle on the visible part of blood vessels is observed mainly for the superficial vessels while deeper inside the body (Fig. 8), the blood vessels are much less clearly outlined and consequently the effect of inclination angle is more difficult to discern.

Minor differences between the phantom experiment and the simulation results, apart from the slightly twisted shape already mentioned in the previous section, can be assigned to the physical constraints present in the experiment: a homogeneous fluence was simulated, to accentuate the influence of anisotropic radiation of cylindrical waves emitted from cylindrical absorbers (e.g., blood vessels).⁵⁵ In the experiment, however, the fluence was depth dependent and was therefore compensated in the reconstruction assuming an exponential optical attenuation for better comparison. Inaccuracies in this assumed distribution of the laser fluence may have led to a changed appearance of the vessel amplitude in addition to the geometry-related differences. In addition, the slight blurring of the vessel image observed in the experiment (~ 0.7 mm apparent vessel diameter) compared to the simulation (~ 0.5 mm apparent vessel diameter) can be

assigned to the acoustic mismatch at the interfaces between the liquid inside the tubing, the tubing material, and the surrounding gelatin, which resulted in short acoustic reverberations. The tubing material itself did not generate any significant signal when filled with water; thus, optical absorption by the tubing material did not contribute to the apparent vessel broadening. Despite the differences, the phantom experiment and simulation consistently showed the inclination angle dependence of the vessel signal.

The vessels in the *in vivo* results (Figs. 7 and 8) show, compared to the phantom results, a more speckled appearance especially at greater depth in the mouse body. Possible reasons for that are inhomogeneous sound speed in the tissue between the vessels and the probe, which probably lead to acoustic aberrations, and thus, to ripples in the propagating wave front. The initially cylindrical wave front would then have looked like as if generated by a string of small spherical optoacoustic sources rather than a continuous line. Additionally, the vasculature network is differently structured deep inside the body, where it feeds the internal organs, branching into fine vascular trees and capillaries. These fine structures, which were below the resolution limit of our optoacoustic imaging system, may have acted as an inhomogeneous distribution of optical absorption without a clear outline. In addition, the contrast resolution at the larger depths was obscured by clutter, owing to the reflection-mode setup required for the mouse experiment.^{33,54,56} In spite of these issues, the *in vivo* results also demonstrate the significant influence of the probe inclination on the imaging outcome.

The cause for the inclination dependence of the amplitude of the vessel signal can also be explained analog to a limited view problem. In the classical limited view problem the lack of data when using a limited aperture array causes loss of image detail.^{40,57-59} In the case of a linear array probe the limited aperture in direction of the 2-D imaging plane leads to loss of visibility of edges depending on the orientation of these edges within the imaging plane. On the contrary, the inclination-dependent loss, showed in this paper, is caused by the lack of data in direction perpendicular to the imaging plane, where the aperture is limited to one single element. This leads for the cylindrical blood vessels to a high dependence of the visibility on the vessel orientation relative to the probe's axial direction.

One important implication of the inclination dependence on the detection sensitivity is the prospects for 2-D optoacoustic imaging using linear array probes. With such probes, a narrow elevation aperture is crucial for selective detection of a 2-D tissue plane. If several blood vessel sections are simultaneously present in the imaging plane, the ones that are oriented perpendicularly relative to the imaging plane are detected the strongest even if they contain less blood than others that are obliquely oriented. Because the blood vessel orientation cannot be determined from a single 2-D image, a quantitative relation between signal amplitude and amount of absorbed energy cannot exist. This can be seen in the simulation results, where the signal amplitude of individual vessels changes significantly by changing the inclination angle from +10 deg to -10 deg, even if the intersection point of the imaging plane with the vessels remains constant (Fig. 6). This prevents quantitative interpretation of the absolute amplitude of the OAI signal detected with a linear probe. Therefore, 2-D measurements relying on the absolute signal amplitude, for example, the determination of the total hemoglobin concentration, are not possible even if the local

fluence is accurately known. Only measurements based on a relative amplitude change, e.g., when changing the irradiation wavelength for spectral imaging of oxygen saturation, can be quantitatively performed.

The inclination dependence also has implications where real-time capability is not required. A previous publication suggested the use of commercial linear array probes for optoacoustic 3-D volume measurement of the vascular network of a human forearm using a fixed setup with controlled probe motion.²³ Experimental imaging was performed at one inclination angle, and, consistent with our results, only those branches of the cephalic vein that were roughly perpendicular to the transducer's axial direction were detected. We have shown that the superposition of scans taken at different inclination angles generates a more complete image of a vessel structure (Video 1). This procedure, however, is time consuming and for a precise superposition of the inclination angle the exact scan position must be known and motion of the scan object must be restrained to avoid artifacts. Alternatively, a scanning linear array or a 2-D array with a wide elevation aperture instead of a plane detectivity allows the detection of randomly oriented vessels without the requirement of multiple scans at different probe inclinations. With such wide elevation aperture probes, a comparably faster scanning and a direct reconstruction of a 3-D volume with high resolution in all directions would be possible. In any case these more complex setups lack the flexibility required for versatile imaging through any part of the body surface and complicate real-time imaging.

For real-time applications our findings take the form of directives to the medical practitioner while using OAI for vasculature imaging. Similar to Doppler US where alignment of the imaging plane parallel to the vessel is required for optimum flow sensitivity, in OAI the imaging plane must be dynamically aligned perpendicular to the blood vessels to generate the strongest signal.

Finally, our findings impact the imaging of other tissue structures having a strong symmetry, such as the interface between fat and muscle tissue or connective tissue layers (plane transients), cysts (spherical transients) when not centered in the imaging plane, tendons (cylindrical transients), etc., at irradiation wavelengths where these structures may take the role as primary source of contrast. In all those examples, strongly directive optoacoustic transients are emitted by the portion of the structure that is located in the imaging plane, and thus the structure may not be detected.

5 Conclusion

When employing a linear array probe with plane detectivity for real-time and free-hand optoacoustic imaging of the vasculature, the signal amplitude strongly depends on the orientation of the blood vessels relative to the imaging plane. Care must therefore be taken to guide the probe such that vessels of interest are scanned at a 90-deg angle in order to be sensitively detected. Therefore, the examination procedure must always involve scanning at a range of angles to ensure that the complete vessel structure has been visualized. In addition, our findings imply that care must be taken in general when interpreting the imaging outcome. Because the signal amplitude in the 2-D image is not determined by the optical absorption alone but as well by the spatial orientation of the tissue structures relative to the imaging plane, a quantitative reconstruction of parameters that depend on absolute signal amplitude, such as total hemoglobin content, is not possible.

Acknowledgments

This research was supported in parts by the Swiss National Science Foundation (No. 205320-103872), by the European Commission's 7th Framework Programme "FULLPHASE" Collaborative Project, ICT-2011, No. 318067, by the Cancer Research UK, and by the Engineering & Physical Sciences Research Council Cancer Imaging Centre grant. We specially thank Fukuda Denshi Switzerland and Zonare Medical Systems Inc., USA, for providing equipment and technical support.

References

- J. H. Stein et al., "Use of carotid ultrasound to identify subclinical vascular disease and evaluate cardiovascular disease risk: a consensus statement from the American Society of Echocardiography Carotid Intima-Media Thickness Task Force. Endorsed by the Society for Vascula," *J. Am. Soc. Echocardiog.* **21**(2), 93–111 (2008).
- T. Iwao et al., "Value of Doppler ultrasound parameters of portal vein and hepatic artery in the diagnosis of cirrhosis and portal hypertension," *Am. J. Gastroenterol.* **92**(6), 1012–1017 (1997).
- S. Gaiani et al., "Assessment of vascular patterns of small liver mass lesions: value and limitation of the different Doppler ultrasound modalities," *Am. J. Gastroenterol.* **95**(12), 3537–3546 (2000).
- H. B. Xiao, S. J. D. Brecker, and D. G. Gibson, "Effects of abnormal activation on the time course of the left ventricular pressure pulse in dilated cardiomyopathy," *Heart* **68**(10), 403–407 (1992).
- H. Masugata et al., "Tissue Doppler echocardiography for predicting arterial stiffness assessed by cardio-ankle vascular index," *Toh. J. Exp. Medicine* **217**(2), 139–146 (2009).
- J. Hung et al., "3D echocardiography: a review of the current status and future directions," *J. Am. Soc. Echocardiog.* **20**(3), 213–233 (2007).
- K. Konno et al., "Liver tumors in fatty liver: difficulty in ultrasonographic interpretation," *Abdom. Imag.* **26**(5), 487–491 (2001).
- J. Baker et al., "Sonography of solid breast lesions: observer variability of lesion description and assessment," *A. J. Roentgenol.* **172**(6), 1621–1625 (1999).
- S. Takiuchi et al., "Diagnostic value of carotid intima-media thickness and plaque score for predicting target organ damage in patients with essential hypertension," *J. Hum. Hyperten.* **18**(1), 17–23 (2004).
- L. Balestrini et al., "Real-time 3-dimensional echocardiography evaluation of congenital heart disease," *J. Am. Soc. Echocardiog.* **13**(3), 0171–0176 (2000).
- A. Heimdal, S. Member, and H. Torp, "Ultrasound Doppler measurements of low velocity blood flow: limitations due to clutter signals from vibrating muscles," *IEEE Trans. Ult. Ferr. Freq. Cont.* **44**(4), 873–881 (1997).
- A. Karabutov, N. B. Podymova, and V. S. Letokhov, "Time-resolved laser optoacoustic tomography of inhomogeneous media," *Appl. Phys. B* **63**(6), 545–563 (1996).
- P. Beard, "Biomedical photoacoustic imaging," *Interface Focus* **1**(4), 602–631 (2011).
- K. H. Song and L. V. Wang, "Deep reflection-mode photoacoustic imaging of biological tissue," *J. Biomed. Opt.* **12**(6), 060503 (2007).
- M. Xu and L. V. Wang, "Photoacoustic imaging in biomedicine," *Rev. Sci. Instrum.* **77**(4), 041101 (2006).
- E. W. Stein, K. Maslov, and L. V. Wang, "Noninvasive, in vivo imaging of blood-oxygenation dynamics within the mouse brain using photoacoustic microscopy," *J. Biomed. Opt.* **14**(2), 020502 (2009).
- I. M. Graf et al., "Noninvasive detection of intimal xanthoma using combined ultrasound, strain rate and photoacoustic imaging," *Ultrason.* **52**(3), 435–441 (2012).
- R. I. Siphanto et al., "Serial noninvasive photoacoustic imaging of neovascularization in tumor angiogenesis," *Opt. Express* **13**(1), 89–95 (2005).
- G. Ku et al., "Thermoacoustic and photoacoustic tomography of thick biological tissues toward breast imaging," *Tech. Canc Res. & Treat.* **4**(5), 559–565 (2005).
- T. D. Khokhlova et al., "Optoacoustic imaging of absorbing objects in a turbid medium: ultimate sensitivity and application to breast cancer diagnostics," *Appl. Opt.* **46**(2), 262–272 (2007).
- J. J. Niederhauser et al., "Combined ultrasound and optoacoustic system for real-time high-contrast vascular imaging *in vivo*," *IEEE Trans. Med. Imag.* **24**(4), 436–440 (2005).
- S. Hu, K. Maslov, and L. V. Wang, "In vivo functional chronic imaging of a small animal model using optical-resolution photoacoustic microscopy," *Med. Phys.* **36**(6), 2320–2323 (2009).
- M. P. Fronheiser et al., "Real-time optoacoustic monitoring and three-dimensional mapping of a human arm vasculature," *J. Biomed. Opt.* **15**(2), 021305 (2010).
- S. Hu and L. V. Wang, "Photoacoustic imaging and characterization of the microvasculature," *J. Biomed. Opt.* **15**(1), 011101 (2010).
- X. Wang et al., "Noninvasive imaging of hemoglobin concentration and oxygenation in the rat brain using high-resolution photoacoustic tomography," *J. Biomed. Opt.* **11**(2), 024015 (2006).
- G. M. Gordillo and C. K. Sen, "Revisiting the essential role of oxygen in wound healing," *Am. J. Surg.* **186**(3), 259–263 (2003).
- H. F. Zhang et al., "Imaging acute thermal burns by photoacoustic microscopy," *J. Biomed. Opt.* **11**(5), 054033 (2006).
- M. Yamazaki et al., "Measurement of burn depths in rats using multi-wavelength photoacoustic depth profiling," *J. Biomed. Opt.* **10**(6), 064011 (2005).
- Y. Lao et al., "Noninvasive photoacoustic imaging of the developing vasculature during early tumor growth," *Phys. Med. Bio.* **53**(15), 4203–4212 (2008).
- J. Jose et al., "Imaging of tumor vasculature using Twente photoacoustic systems," *J. Biophoton.* **2**(12), 701–717 (2009).
- G. F. Lungu et al., "In vivo imaging and characterization of hypoxia-induced neovascularization and tumor invasion," *Int. J. Oncol.* **30**(1), 45–54 (2007).
- S. Mallidi, G. P. Luke, and S. Emelianov, "Photoacoustic imaging in cancer detection, diagnosis, and treatment guidance," *Tren. Biotech.* **29**(5), 213–221 (2011).
- M. Jaeger et al., "Reduction of background in optoacoustic image sequences obtained under tissue deformation," *J. Biomed. Opt.* **14**(5), 054011 (2009).
- R. G. M. Kolkman et al., "Real-time *in vivo* photoacoustic and ultrasound imaging," *J. Biomed. Opt.* **13**(5), 050510 (2008).
- S. W. Smith, "High-speed ultrasound volumetric imaging system-part I: transducer design and beam steering," *IEEE Trans. Ult. Ferr. Freq. Cont.* **38**(2), 100–108 (1991).
- M. F. Rasmussen et al., "Comparison of 3D synthetic aperture imaging and explosivescan using phantom measurements," in *Proceedings of IEEE International Ultrasonics Symposium 2012*, pp. 3–7, IEEE, Dresden, Germany (2012).
- K. P. Köstli et al., "Optoacoustic imaging using a three-dimensional reconstruction algorithm," *IEEE J. Sel. Top. Electron.* **7**(6), 918–923 (2001).
- M. Xu and L. Wang, "Universal back-projection algorithm for photoacoustic computed tomography," *Phys. Rev. E* **71**(1), 016706 (2005).
- M. Jaeger et al., "Fourier reconstruction in optoacoustic imaging using truncated regularized inverse k-space interpolation," *Inv. Prob.* **23**(6), S51–S63 (2007).
- Y. Xu et al., "Reconstructions in limited-view thermoacoustic tomography," *Med. Phys.* **31**(4), 724 (2004).
- M. Xu and L. V. Wang, "Time-domain reconstruction for thermoacoustic tomography in a spherical geometry," *IEEE Trans. Med. Im.* **21**(7), 814–822 (2002).
- Y. Xu, M. Xu, and L. V. Wang, "Exact frequency-domain reconstruction for thermoacoustic tomography—II: cylindrical geometry," *IEEE Trans. Med. Im.* **21**(7), 829–833 (2002).
- R. Ma et al., "Non-invasive whole-body imaging of adult zebrafish with optoacoustic tomography," *Phys. Med. Bio.* **57**(22), 7227–7237 (2012).
- D. Razansky, C. Vinegoni, and V. Ntziachristos, "Imaging of mesoscopic-scale organisms using selective-plane optoacoustic tomography," *Phys. Med. Bio.* **54**(9), 2769–2777 (2009).
- R. G. M. Kolkman et al., "Photoacoustic imaging of blood vessels with a double-ring sensor featuring a narrow angular aperture," *J. Biomed. Opt.* **9**(6), 1327–1335 (2004).
- R. G. M. Kolkman, W. Steenbergen, and T. G. van Leeuwen, "In vivo photoacoustic imaging of blood vessels with a pulsed laser diode," *Las. Med. Sci.* **21**(3), 134–139 (2006).

47. K. P. Köstli and P. C. Beard, "Two-dimensional photoacoustic imaging by use of Fourier-transform image reconstruction and a detector with an anisotropic response," *Appl. Opt.* **42**(10), 1899–1908 (2003).
48. R. A. Kruger et al., "Thermoacoustic computed tomography using a conventional linear transducer array," *Med. Phys.* **30**(5), 856–860 (2003).
49. G. Diebold, T. Sun, and M. Khan, "Photoacoustic monopole radiation in one, two, and three dimensions," *Phys. Rev. Lett.* **67**(24), 3384–3387 (1991).
50. H. G. Akarçay et al., "Determining the optical properties of a gelatin-TiO(2) phantom at 780 nm," *Biomed. Opt. Exp.* **3**(3), 418–434 (2012).
51. G. M. Spirou et al., "Optical and acoustic properties at 1064 nm of polyvinyl chloride-plastisol for use as a tissue phantom in biomedical optoacoustics," *Phy. Med. Bio.* **50**(14), N141–N153 (2005).
52. I. Calasso, W. Craig, and G. Diebold, "Photoacoustic point source," *Phys. Rev. Lett.* **86**(16), 3550–3553 (2001).
53. "American National Standard for Safe Use of Lasers: ANSI Z136.1—2007," Laser Institute of America, Orlando, Florida (2007).
54. M. Jaeger et al., "Improved contrast deep optoacoustic imaging using displacement-compensated averaging: breast tumour phantom studies," *Phys. Med. Biol.* **56**(18), 5889–5901 (2011).
55. M. I. Khan and G. J. Diebold, "The photoacoustic effect generated by laser irradiation of an isotropic solid cylinder," *Ultrason.* **34**(1), 19–24 (1996).
56. M. Jaeger et al., "Deformation-compensated averaging for clutter reduction in epiphotoacoustic imaging in vivo," *J. Biomed. Opt.* **17**(6), 066007 (2012).
57. T. Sato et al., "Tomographic image reconstruction from limited projections using iterative revisions in image and transform spaces," *Appl. Opt.* **20**(3), 395–399 (1981).
58. S. Ma, S. Yang, and H. Guo, "Limited-view photoacoustic imaging based on linear-array detection and filtered mean-backprojection-iterative reconstruction," *J. Appl. Phys.* **106**(12), 123104 (2009).
59. G. Paltauf et al., "Experimental evaluation of reconstruction algorithms for limited view photoacoustic tomography with line detectors," *Inv. Probl.* **23**(6), S81–S94 (2007).